*Korean J. Chem. Eng.*, 39(10), 2652-2663 (2022)
DOI: 10.1007/s11814-022-1198-9

pISSN: 0256-1115
eISSN: 1975-7220

# Vapor-phase hydrogenolysis of glycerol to value-added 1,2-propanediol over copper-nickel bimetallic catalysts supported on activated carbon

**Mohammad Kashif*, Sadhasivam Thangarasu*, Tae Hwan Oh*,†, Prakash Biswas**, and Dohyung Kang***

*School of Chemical Engineering, Yeungnam University, Gyeongsan 38541, Korea
**Department of Chemical Engineering, Indian Institute of Technology Roorkee, 247667 Roorkee, Uttarakhand, India
(*Received 21 January 2022 • Revised 30 May 2022 • Accepted 2 June 2022*)

**Abstract**−In the production of biodiesel, a sustainable energy alternative to fossil fuel, surplus glycerol, is generated as a by-product. Valorization of excess glycerol is the most promising approach for rendering the biodiesel sector fiscally practical. Herein, copper and nickel monometallic and bimetallic catalysts supported over activated carbon were developed using the incipient wetness impregnation technique for the hydrogenolysis of vapor-phase glycerol to 1,2-propanediol (1,2-PDO) at a pressure of 0.75 MPa and temperature of 220 °C. The catalysts were characterized by Brunauer-Emmett-Teller, X-ray diffraction, $H_2$-temperature-programmed reduction, $NH_3$-temperature-programmed desorption, X-ray photoelectron spectroscopy, and scanning electron microscopy analyses. The bimetallic catalysts afforded higher product yields than the monometallic catalysts did in glycerol hydrogenolysis. Cu-Ni(1 : 1)/AC gave the maximum yield of 1,2-PDO (87.3%), with high glycerol conversion (95.7%) under the previously mentioned reaction conditions, with a comparatively low molar ratio of hydrogen to glycerol (54.6). The strong copper-nickel synergy, smaller crystallite size, and high acid strength of Cu-Ni(1 : 1)/AC account for this superior performance.

Keywords: Glycerol, Hydrogenolysis, Acetol, Hydrogenation, Dehydration, Catalyst

## INTRODUCTION

Based on the report of Renewable Energy Policy Network for the 21st Century (REN 21) published in 2021, global biodiesel production has increased to 46.8 billion liters in 2020 [1]. Due to the various advantages of biodiesel, global production reached 36 billion liters in 2017, with a projected rise of 9% by 2027 [2]. Biodiesel is predominantly prepared by transesterification of triglycerides, which generates excess glycerol (~10 wt%) as a byproduct. The massive influx of glycerol in the market has resulted in a steep drop in its price, putting the economic viability of the biodiesel industry in jeopardy [3,4]. Therefore, developing a commercially sustainable method to process raw glycerol into value-added products is vital for the biodiesel industry. Among the several methodologies explored for glycerol valorization, selective hydrogenolysis of glycerol to 1,2-propanediol (1,2-PDO) has proven to be a potential approach due to the economic significance of 1,2-PDO, as well as the cost-effectiveness and environmental friendliness of the process [5-9]. A schematic diagram of the glycerol hydrogenolysis reaction pathways is presented in Fig. 1. Glycerol is converted to 1,2-PDO in two steps, with the first step being glycerol transformation to acetol via catalytic dehydration over the acid sites of the catalyst. The subsequent step involves the transformation of acetol to 1,2-PDO via hydrogenation over active metal sites [10-14].

Numerous noble and transition metals have been widely researched for glycerol hydrogenolysis in the liquid phase [15-20]. Noble metals promote C-C bond scission, resulting in excess glycerol hydrogenolysis to form degradation products, such as methane and ethylene glycol (EG), which lowers the 1,2-PDO selectivity [15-17]. In transition metals, copper-based catalysts have demonstrated efficient performance and product selectivity as they promote C-O bond scission in the presence of hydrogen [21-26]. Copper-based catalysts with various supports, such as SBA-15 [24], MgO [27,29,30], $\gamma$-$Al_2O_3$ [21,31], boehmite [28], $SiO_2$ [32], and $CeO_2$ [33], showed high selectivity towards 1,2-PDO under various conditions, resulting in numerous advantages [39-42]. However, the poor thermal stability of copper catalysts has stymied their industrialization [21]. Apart from Cu catalysts, Ni-based catalysts have also been reported for the improved hydrogenolysis reaction. These catalysts promote C-C scission, resulting in excessive glycerol decomposition to produce ethylene glycol and lower alcohols. Ni catalysts are advantageous because they promote the hydrogenation-dehydrogenation reaction, which is essential for the synthesis of acetol during glycerol hydrogenolysis [40,43,44]. However, compared to noble metal catalysts, Ni-based catalysts have lower stability because they are susceptible to pore blockage by carbon deposition. Several studies have proposed that bimetallic catalysts have superior performance and selectivity due to strong synergic interactions between the metal and supports and the bifunctional effects of acidic or basic sites with metallic sites [29-31]. Despite extensive research, liquid-phase glycerol hydrogenolysis has several limitations, such as high hydrogen pressure (1.0-10.0 MPa), lengthy reaction time (5.0-30.0 h), easy formation of by-products, structural harm to catalysts, and catalyst leaching [27,33-38]. Consequently, gas-phase glycerol hydrogenolysis in a packed bed continuous flow reactor has recently garnered considerable interest. To date, research on the production of 1,2-PDO via gas-phase glycerol hydrogenolysis remains scarce.

The most prominent features for a suitable catalyst support are

†To whom correspondence should be addressed.
E-mail: taehwanoh@ynu.ac.kr

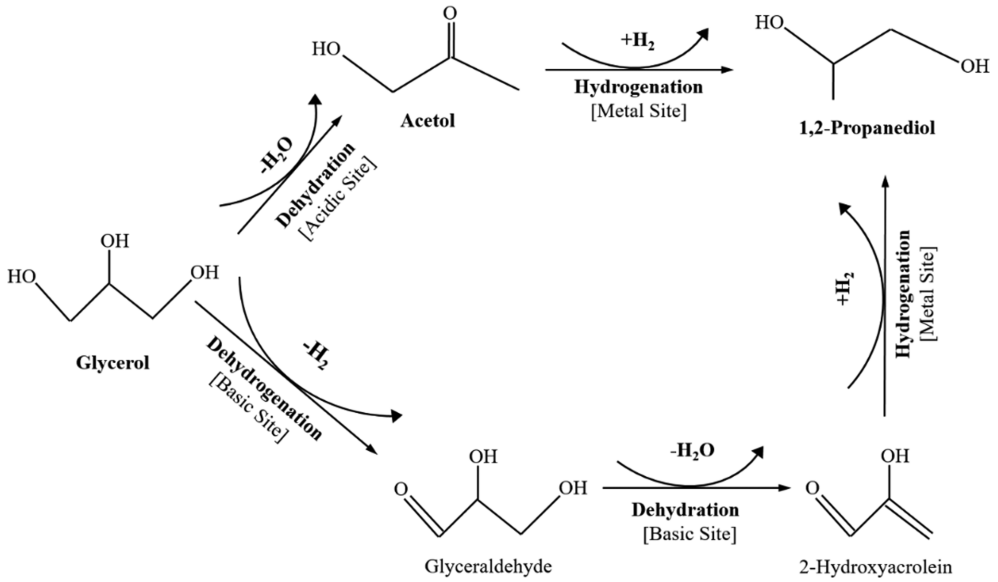


**Fig. 1. Reaction pathways for glycerol hydrogenolysis.**

a large surface area, high porosity, inertness, stability under the reaction conditions, regenerability, favorable mechanical features, and the ability to conform their physical shape to a specific reactor [45-48]. Among the different catalyst support materials, carbon-structured materials can be considered as an efficient catalyst support material because of their intrinsic properties and surface phenomenon [45]. In this regard, activated carbon has a non-graphitizable turbostratic microstructure, resulting in a high affinity for oxygen chemisorption, and possesses acidic surface oxygenated groups [49]. Studies on carbon structures as catalyst support materials for vapor-phase glycerol hydrogenolysis are still scarce. From this perspective, the pivotal goal of this study was to develop a new catalyst system for the selective hydrogenolysis of glycerol to 1,2-PDO while maintaining mild reaction conditions. Bimetallic copper and nickel catalysts supported on activated carbon for vapor-phase glycerol hydrogenolysis to commercially valuable compounds like 1,2-PDO were investigated. The impact of the copper-nickel mass ratio on the physicochemical parameters and catalytic activity was analyzed. The effects of several reaction parameters were also examined to optimize the glycerol conversion and product selectivity. It is shown that bimetallic catalysts afford higher product yields than the monometallic catalysts in glycerol hydrogenolysis, and the strong copper-nickel synergy, smaller crystallite size, and high acid strength of the Cu-Ni(1 : 1)/AC provide superior performance.

## EXPERIMENTAL

### 1. Materials

$Cu(NO_3)_2{\cdot}3H_2O$ (purity 99.5%, Daejung Chemicals, South Korea) and $Ni(NO_3)_2{\cdot}6H_2O$ (purity 99.9 %, Sigma Aldrich, South Korea) were used as metal precursors, with activated carbon (TCI Chemicals, South Korea/Himedia Chemicals Pvt. Ltd., India) serving as a catalyst support. 1,3-Propanediol (purity 99%, Sigma Aldrich Private Ltd. India), 1,2-propanediol (purity 99%, Merck Specialities Private Ltd., India), acetol (purity 95%, Alfa Aesar Private Ltd., India), and glycerol (purity 99%, Merck Specialities Private Ltd., India) were used for product calibration and as the feed, respectively. High-purity nitrogen (99.999%) and hydrogen (99.999%) were obtained from Sigma Gases, India, and required no additional purification before use.

### 2. Method of Preparation

Diverse monometallic and bimetallic copper-nickel catalysts on activated carbon supports, with a constant metal content (20 wt%), were developed by a conventional incipient wetness impregnation process. Bimetallic catalysts, such as 3 : 1, 1 : 1, and 1 : 3, were prepared using different Cu : Ni mass ratios. A mixture of a prescribed quantity of metal precursor salts, Millipore deionized water, and a fixed amount of activated carbon as a porous support was stirred continuously for 20 min. Afterward, the resulting slurry was left to age overnight at room temperature before being dried at 110 °C for 12 h to remove moisture. The catalysts were then calcined at 300 °C for 5 h under an inert atmosphere (He).

### 3. Catalyst Characterization

The physicochemical parameters of the catalysts were determined by various methods, including nitrogen adsorption-desorption, X-ray diffraction (XRD), X-ray photoelectron spectroscopy (XPS), hydrogen temperature-programmed reduction ($H_2$-TPR), and ammonia temperature-programmed desorption ($NH_3$-TPD) to elucidate the Cu-Ni interaction and catalytic activity. The morphology and elemental composition of the catalysts were recorded using field-emission scanning electron microscopy (FE-SEM). The surface area, pore size distribution, and pore volume were determined via nitrogen adsorption-desorption analyses at the boiling point of liquid nitrogen (−196 °C) using a physisorption analyzer (3-FLEX; Micromeritics) at Core Research Support Center for Natural Products and Medical Materials in Yeungnam University. All catalyst samples were outgassed at 300 °C for 6 h before being analyzed. For the Brunauer-Emmett-Teller (BET) surface area calculations, the relative pressure ($P/P_o$) was varied between 0.05 and 0.3. The pore volume and pore size distribution were computed

using the Barrett-Joyner-Halenda (BJH) method with Halsey-Faas correction by considering the desorption branch of the isotherms. X-ray diffraction (XRD) spectra were obtained using a Bruker AXS D8 Advance diffractometer with a Cu-K$\alpha$ monochromatic light source ($\lambda$=0.154 nm) over a scanning angle ($2\theta$) range of 10-90° with a constant time of 3 s and a scanning rate of 0.02° $s^{-1}$. Based on the linewidth of the XRD peaks equivalent to the corresponding crystal planes of NiO and CuO, the Scherrer equation was used to compute the mean crystallite sizes of NiO and CuO. The reduction behavior of the catalysts was investigated by $H_2$-TPR analysis on a Microtrac Belcat II analyzer with a thermal conductivity detector (TCD). Generally, the catalyst sample (50 mg) was dried overnight in an oven at 120 °C before the TPR study. The dry catalyst was pretreated for 2 h at 150 °C in a U-shaped quartz reactor under nitrogen flow (30 $cm^3$ $min^{-1}$) and then cooled to ambient temperature. The pretreated sample was heated from 25 °C to 900 °C with a temperature ramp of 1 °C/min under 5% $H_2$ in argon (20 $cm^3$ $min^{-1}$) flow. A cold trap immersed in liquid $N_2$ and isopropanol slurry was used to condense the vapors generated during the reduction, and the $H_2$ concentration in the discharge stream was recorded by the TCD. The acidic nature of the synthesized catalysts was examined by $NH_3$-TPD analyses using a Micromeritics Pulse Chemisorb 2720 instrument coupled with a TCD. First, the catalyst sample (100 mg) was degassed under helium flow (20 cc $min^{-1}$) for 2 h at 150 °C before cooling to room temperature. The pretreated sample was saturated for 1 h with a 27% $NH_3$-helium gas mixture (30 ml $min^{-1}$), followed by purging with helium (20 $cm^3$/min) for the next 1 h to remove excess $NH_3$. The catalyst sample was further heated from 30 °C to 850 °C at a temperature ramp of 10 °C/min while the TCD signals were continuously monitored for $NH_3$ desorption. X-ray photoelectron spectroscopy (XPS) was used to explore the chemical composition and electronic states of the catalysts. XPS experiments were conducted using monochromatic Al-K$\alpha$ radiation, on a Thermo Scientific ESCALAB 220iXL instrument. The binding energy was calibrated by referencing the main adventitious C1s line at 284.7 eV, resulting in an experimental error within ±0.1 eV. A concentric hemispherical analyzer functioning in the consistent flow energy mode (29.35 eV) with an analysis area of 720 mm reported high-resolution bands at a take-off angle of 45°. The analysis chamber was maintained at a pressure of less than $5\times10^{-6}$ Pa. The peak maxima and regions were evaluated by fitting the spectra to Gaussian-Lorentzian curves. The element concentrations in the near-surface area were determined by normalizing the peak areas with Scofield sensitivity variables using the spectrometer's transmission mode. The collected data were analyzed by subtracting the nonlinear Shirley-like background from the spectral signals. Scanning electron microscopy (SEM) was used to assess the morphological features and metal distribution of the developed catalysts, combined with energy-dispersive X-ray (EDX) analysis to determine the local elemental concentration of the two metal ions in the case of the bimetallic catalysts. A field-emission scanning electron microscope (Hitachi S-4800, Tokyo, Japan) with EDX (EDS, Horiba EMAX, Horiba Co., Ltd., Kyoto, Japan) was used to collect the SEM images. The sample was uniformly dispersed all over the sample holder and plated with carbon using a sputter coater. SEM images were acquired under vacuum at an escalated potential of 10 kV, with a scanning energy range of 0-10 keV for EDS analysis and a time lapse of 100 s.

**4. Catalytic Test**

The experiments were run in a stainless steel continuous packed bed down-flow tubular reactor with an inner diameter of 12.5 mm and a length of 540 mm (Chemito Technologies, India). The reactor was heated using a tube furnace equipped with a programmed temperature control. The reactor also featured pressure indicators and thermocouples for detecting the inside and outside temperatures, along with a mass flow controller for regulating the input gas flow. A preheater and a liquid feed pump of capacity 0.01-9.9 $cm^3$/min at 10 MPa pressure (Lab Alliance, USA) were linked to the reactor inlet. A gas-liquid separator (Model No. FL300, Julabo, Germany) was connected via a recirculating condenser across the reactor. The catalyst samples were first compressed into 20 mm diameter round pellets and then split into small fragments. Typically, the synthesized catalyst was sandwiched between two layers of glass wool within a constant-temperature section of the reactor. Before each experiment, the catalysts were reduced *in-situ* under a pure hydrogen stream (50 ml/min) for 3 h at the reduction temperature observed from the TPR measurements. Initially, the reactor was pressurized using a back-pressure valve connected to the reactor outlet. An aqueous glycerol solution (20 wt%) was continuously pumped by a liquid feed pump immediately after the reaction system was cooled to the appropriate temperature and pressure. The glycerol feed was vaporized by passing through an evaporator at 250 °C before being fed to the reactor. A mixture consisting of vaporized glycerol feed, hydrogen (100 $cm^3$ $min^{-1}$), and nitrogen (20 $cm^3$ $min^{-1}$) as an inert gas, was introduced through the reactor inlet. The operating conditions were kept at 220 °C, 0.75 MPa, 4.0 g catalyst, WHSV of 0.97 $h^{-1}$, aqueous feed with 20 wt% glycerol, and $H_2$ to glycerol mole ratio of 54.6. The reaction parameters were studied by varying the temperature, pressure, and catalyst amount in the range of 220-300 °C, 0.2-1.0 MPa, and 1-6 g, sequentially. The gaseous and liquid products were received in a gas-liquid separator, and then cooled in a recirculating condenser maintained at 5 °C. The condensed products were collected and evaluated by a gas chromatograph (Newchrom 6800 GC instrument) in offline mode, fitted with a Chromosorb-101 packed column (1.52 m× 2 mm ID×3.1 mm OD) and a flame ionization detector (FID). The selectivity of the product was determined using an internal standard (*n*-butanol). All reported results agreed, with a carbon balance within ±5% of 100%.

The equations below were used to determine the feed conversion, selectivity to the products, and product yields.

$$\text{Conversion (\%)} = \frac{\text{Moles of glycerol converted}}{\text{Total glycerol moles in the feed}} \times 100$$

$$\text{Selectivity (\%)} = \frac{\text{Carbon moles in the specific product}}{\text{Total moles of carbon in all liquid products}} \times 100$$

$$\text{Yield (\%)} = \text{Conversion (\%)} \times \text{Selectivity (\%)}$$

The weight hourly space velocity (WHSV) is determined by the following relationship

$$\text{WHSV } (h^{-1}) = \frac{\text{Hourly Mass Feed Flowrate (g/h)}}{\text{Mass of catalyst (g)}}$$

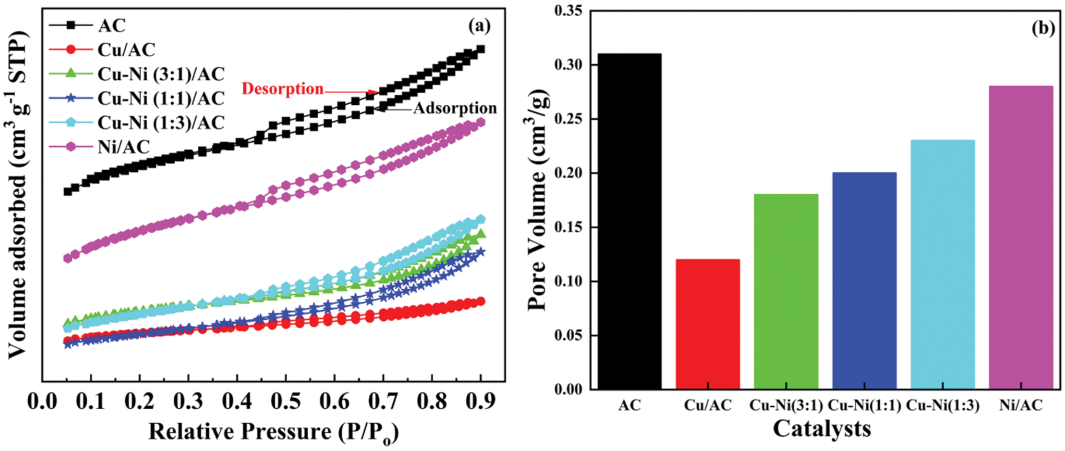


**Fig. 2. (a) Nitrogen physisorption isotherms of the calcined catalysts (b) Variation of pore volume of the freshly synthesized catalysts.**

**Table 1. Physico-chemical parameters of the calcined catalysts**

| Catalyst | $S_B$ ($m^2/g$)[a] | $V_P$ ($cm^3/g$)[a] | $D_P$ (nm)[a] | Mean crystallite size (nm)[b] Calcined | | Overall acidic strength (mmol $NH_3$/g(catalyst))[c] |
|---|---|---|---|---|---|---|
| | | | | CuO | NiO | |
| Activated Carbon (AC) | 643 | 0.31 | 4.1 | - | - | 0.83 |
| Cu/AC | 147 | 0.12 | 4.0 | 31 | - | 7.52 |
| Cu-Ni(3 : 1)/AC | 216 | 0.18 | 4.7 | 21.1 | 10.8 | 3.83 |
| Cu-Ni(1 : 1)/AC | 154 | 0.20 | 5.1 | 22.6 | 17.6 | 3.45 |
| Cu-Ni(1 : 3)/AC | 217 | 0.23 | 4.6 | 21.2 | 6.8 | 1.26 |
| Ni/AC | 468 | 0.28 | 3.7 | - | 8.4 | 5.65 |

[a]$N_2$ adsorption-desorption isotherm data. [b]XRD data. [c]$NH_3$-TPD data.

[For 4 g catalyst and an hourly feed flowrate of 4.4 g/h, WHSV is 1.1 $h^{-1}$]

## RESULTS AND DISCUSSION

### 1. BET Surface Area

Fig. 2(a) shows the $N_2$ physisorption isotherms of various mono- and bimetallic catalysts supported on activated carbon. The isotherm of the activated carbon support showed no discernible shift, suggesting that the characteristic morphology of the support was preserved in all the catalysts. The isotherms of all catalyst samples were akin to type IV of the IUPAC classification, corresponding to capillary condensation in uniform mesopores, indicating the mesoporous structure of the catalysts. As shown in Fig. 2(a), a prominent H4-type hysteresis loop was observed within the relative pressure range of $0.9>P/P_o>0.4$, suggesting the presence of plate-like particle aggregates or agglomerates with small slit-like pores in the catalysts, with a large pore volume and a uniform pore size distribution [50,51].

The textural properties of the freshly prepared catalysts, such as the BET surface area ($S_B$), the cumulative pore volume ($V_P$), and Barrett-Joyner-Halenda (BJH) pore diameter ($D_P$), evaluated from the nitrogen adsorption-desorption isotherms are illustrated in Table 1. The pore volumes and BET surface area of the pristine activated carbon support were 0.306 $m^3\ g^{-1}$ and 643 $m^2\ g^{-1}$, respectively. The BET surface areas of the catalysts with varying metal concentrations ranged from 147 to 468 $m^2\ g^{-1}$, suggesting a substantial reduction in the surface area due to blockage of the support pores by larger crystallites, as confirmed by the pore size distribution and hereinafter by the X-ray diffraction (XRD) results. Because of the higher nickel particle dispersion and smaller crystallite size, the monometallic nickel catalyst had the highest surface area (468 $m^2\ g^{-1}$) of all the catalyst samples tested, whereas the monometallic copper catalyst had the lowest value (147 $m^2\ g^{-1}$). All catalysts had pore diameters ranging from 3.7 to 5.1 nm. Due to structural failure of the precursors during the thermal treatment, the pore volume of the catalysts (0.12-0.28 $cm^3\ g^{-1}$) was smaller than that of activated carbon (0.31 $cm^3\ g^{-1}$) [21,52]. The average pore diameter and overall pore size of the catalysts are displayed in Table 1.

### 2. X-Ray Diffraction (XRD) Analysis

The crystalline phases and crystal structures of the catalysts were evaluated using XRD. Fig. 3(a) illustrates the XRD spectra of the calcined copper-nickel catalysts supported on activated carbon. The monometallic Cu/AC catalyst shows discrete high-intensity peaks at $2\theta$=61.6°, 48.8°, 38.7°, and 35.5°, corresponding to the ($\bar{1}13$), ($\bar{2}02$), (111), and (002) crystal planes of monoclinic CuO, respectively (JCPDS: 80-1917). CuO exists in the crystalline phase, as indicated by the sharp peaks in the XRD pattern of the Cu/AC catalyst [21]. The XRD spectra reveal that the pristine activated carbon support was amorphous. A distinct sharp peak appears at

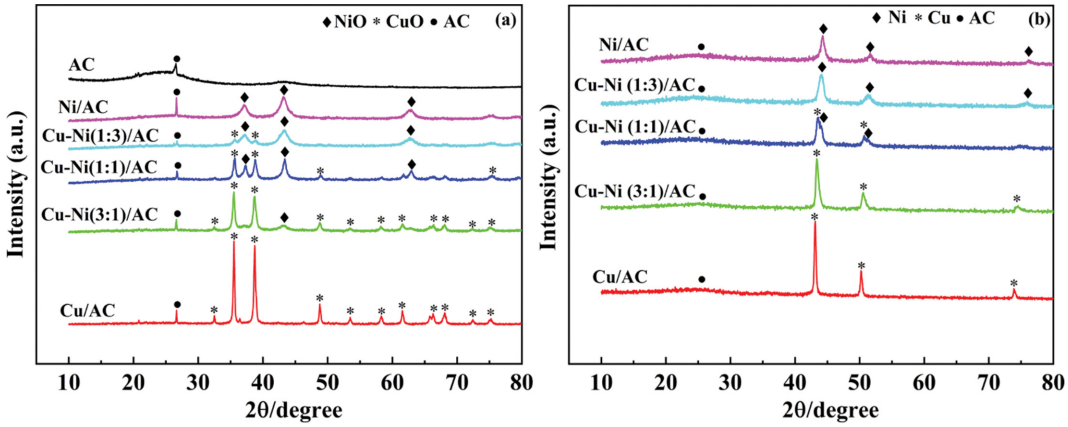


**Fig. 3. XRD patterns of (a) the fresh calcined catalysts and support (b) the fresh reduced catalysts.**

$2\theta$=26.5° for each catalyst, corresponding to the (002) crystal planes of the hexagonal graphite phase of carbon (JCPDS: 41-1487). The peaks at $2\theta$=62.8°, 43.3°, and 37.2°, correspond to the (110), (012), and (101) crystal planes of NiO, respectively (JCPDS: 44-1159), with a typical rhombohedral structure, as shown in the XRD pattern of the Ni/AC catalyst. CuO exhibits sharper and more intense peaks than NiO, indicating that CuO is crystalline and has a larger crystallite size than NiO. The intensity of the CuO peaks decreases with decreasing copper loading, showing that CuO exists as smaller particles at lower copper concentrations and as agglomerates in the bulk at higher copper concentrations [29,53]. For the bimetallic catalysts, the CuO and NiO peaks are less intense and broader than for the monometallic catalysts, demonstrating improved metal oxide dispersion on the activated carbon support in the bimetallic catalysts [21,53]. The average crystallite sizes for CuO and NiO were computed from the Scherrer equation predicated on the line-width from the corresponding XRD peaks, along with the results displayed in Table 1. The CuO crystallite size is in the range of 21-31 nm, whereas the NiO particle size is within 6.5-11 nm. This illustrates that Ni was considerably better dispersed than Cu, which is consistent with the X-ray photoelectron spectroscopy (XPS) measurements [53]. In comparison with the monometallic Cu/AC catalysts, the peak of CuO for the bimetallic Cu-Ni/AC catalysts become broader and less intense as the Ni loading increases, suggesting that the Cu-Ni/AC catalysts comprise smaller crystallites due to limited crystal growth under space constraints [54,55]. The Cu-Ni/AC catalysts have smaller crystallite sizes than the Cu/AC catalysts, indicating that the assimilation of smaller Ni particles results in a smaller CuO particle size. This is in agreement with the assertions of previous authors that $Ni^{2+}$ preferentially occupies octahedral sites [56]. The XRD diffraction patterns of the reduced catalysts can be seen in Fig. 3(b). All the catalysts are reduced at 500 °C for 1 hour. Major peaks of metallic copper are detected in Cu/AC and Cu-Ni/AC at $2\theta$ values of 43.1, 50.2, and 73.9, which correspond to (111), (200), and (220) crystal planes, respectively (JCPDS: 85-1326). The XRD patterns of Cu-Ni/AC and Ni/AC display peaks for metallic Ni at the $2\theta$ values of 44.3, 51.6, and 76.2, which correspond to the (111), (200), and (220) crystal planes of cubic Ni structure (JCPDS: 04-0850). Thus, it confirms the presence of pure metallic form in the reduced catalysts.

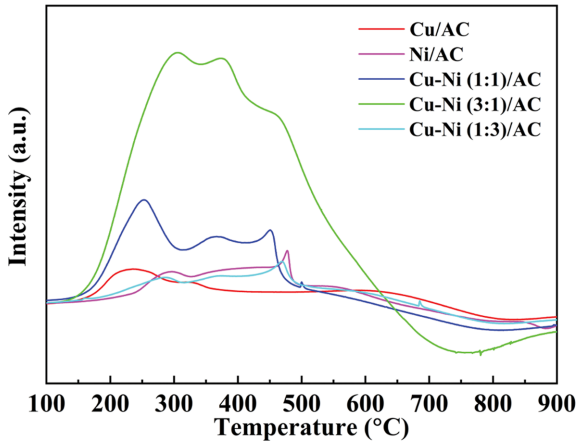


**Fig. 4. $H_2$-TPR profile of freshly calcined catalysts.**

### 3. Hydrogen-Temperature Programmed Reduction (TPR- $H_2$)

The catalysts were pre-reduced to obtain active metal sites for the hydrogenation stage of the process. Fig. 4 shows the TPR data, which were used to determine the pre-reduction temperature for the freshly calcined catalysts. The monometallic Cu catalyst displays two different reduction peaks: a primary broad peak at 236 °C and another intermediate less intensity peak at 319 °C. The lower-temperature peak corresponds to the reduction of well-dispersed CuO species on activated carbon, whereas the higher-temperature peak indicates reduction of the CuO species in the bulk [21,53]. According to prior work, bulk CuO has exhibited a two-step reduction. The first step involved the reduction of CuO to $Cu_2O$, after which $Cu_2O$ was reduced to metallic copper ($Cu^0$) in the second step [21,53]. TPR spectra for the monometallic Ni/AC catalyst reveal a sharp spike at 478 °C and a broad shoulder peak at 296 °C. The broad peak corresponds to the reduction of highly dispersed $Ni^{2+}$ to $Ni^0$, whereas the high-intensity peak at 478 °C suggests the presence of bulk NiO particles interacted strongly with the activated carbon support [21,69]. The TPR profile of the bimetallic catalysts is different from that of the monometallic counterparts, indicating a more complicated reduction process. When compared to monometallic Ni/AC catalysts, the reduction peaks of nickel oxide in bimetallic catalysts shift to lower temperatures with increase in

copper concentration, suggesting that copper assists in NiO reduction. The explanation for this could be that the synergistic interaction of copper and nickel enhances the reducibility by lowering the reduction activation energy for NiO [58,63]. The existence of an additional peak around 370 °C in the TPR profiles of all bimetallic catalysts which is not present in monometallic samples also demonstrates strong synergy between copper and the nickel oxides, and the formation of bimetallic Cu-Ni alloy species [57,58]. The broad peak observed at high temperature (>500 °C) for each catalyst indicates partial gasification of the carbon support due to the reaction of C and $H_2$, leading to methane formation [63,58].

**4. $NH_3$-Temperature Programmed Desorption ($NH_3$-TPD)**

The acidity of catalysts is widely acknowledged to have a major impact on their performance during glycerol hydrogenolysis. Fig. 5 shows the TPD patterns of the freshly calcined catalysts. Based on the quantity of desorbed ammonia, Table 1 shows a quantitative approximation of the distribution of acidic sites in various temperature zones. All catalysts have a distribution of acidic sites in three distinct zones, where three distinct ammonia desorption peaks are observed in the temperature ranges of 100-250 °C, 250-500 °C, and 500-700 °C. The peak in region I (100-250 °C) is associated with $NH_3$ desorption from weak acid sites, whereas the peak in the region II (250-500 °C) is ascribed to moderately strong acid sites. Finally, the third peak (500-700 °C) corresponds to ammonia desorption from strong acid sites [21,59,60]. The $NH_3$-TPD profiles of the support and the catalysts indicate weak and strong acidic sites, as well as a minor peak of medium-strength acidic sites in the bimetallic catalysts. The monometallic catalysts have higher acid strengths than the bimetallic catalysts, in the following order: Cu/AC>Ni/AC>Cu-Ni(3 : 1)/AC>Cu-Ni(1 : 1)/AC>Cu-Ni(1 : 3)/AC.

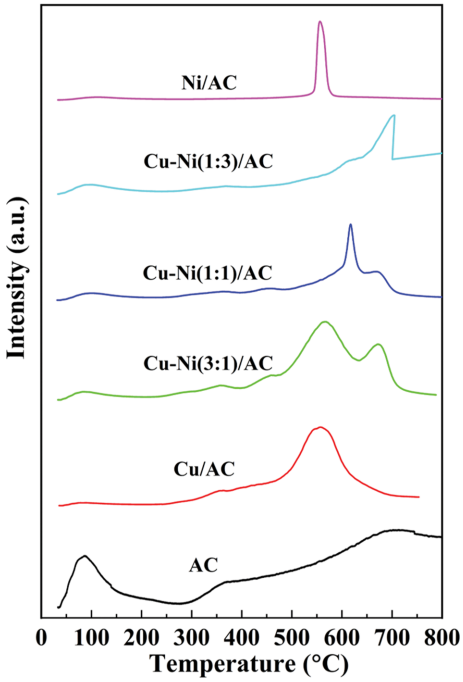


**Fig. 5. $NH_3$-TPD profiles of the support and calcined catalysts.**

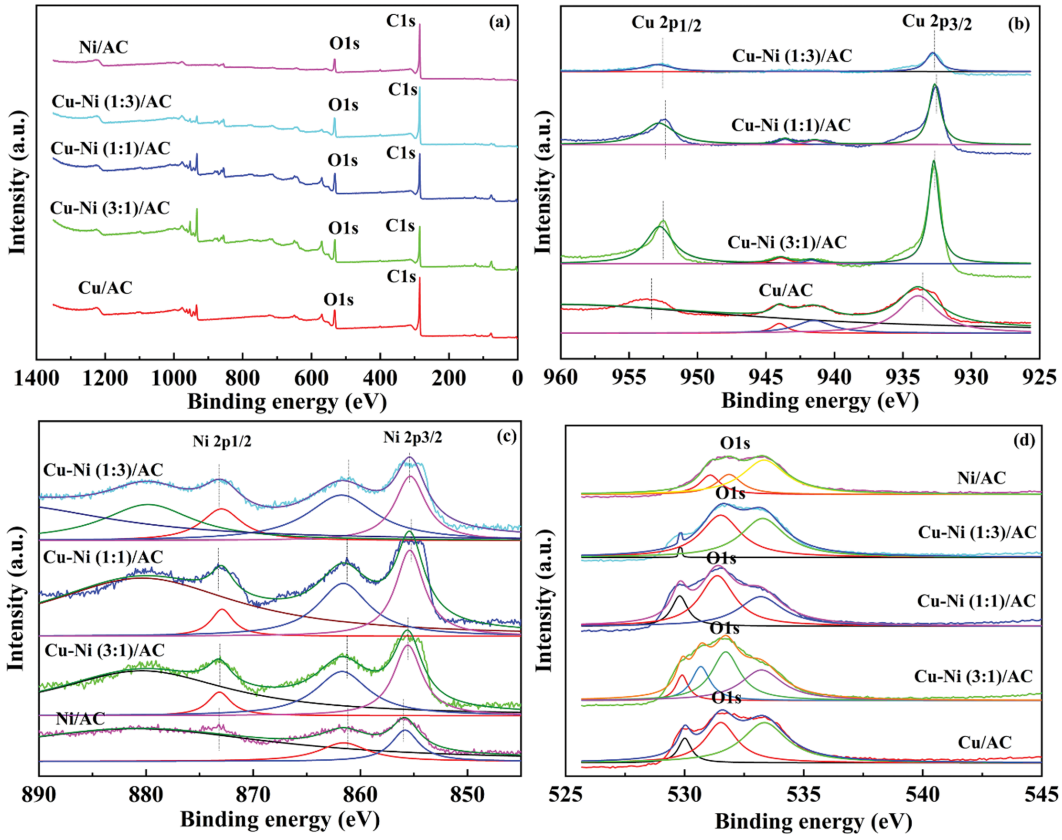


**Fig. 6. XPS profiles for the calcined catalysts (a) XPS spectra, (b) Cu2p peaks, (c) Ni2p peaks, and (d) O1s peak.**

The Cu/AC catalyst has the highest acid strength of 7.52 mmol $NH_3$ $gcat^{-1}$, whereas Cu-Ni(1 : 3)/AC has the lowest acidity (1.26 mmol $NH_3$ $gcat^{-1}$). The lower acidity values of the bimetallic catalysts are attributed to the synergetic interaction between the metals and the support.

**5. X-Ray Photoelectron Spectroscopy (XPS)**

The chemical oxidation states of the calcined catalysts were assessed using X-ray photoelectron spectroscopy (XPS), as shown in Fig. 6. The Cu2p spectra for both monometallic and bimetallic catalysts can be seen in the XPS plots of the calcined catalysts, as shown in Fig. 6(b). The profile of the copper monometallic catalysts exhibits two peaks at 933.4 eV and 953.4 eV for $Cu2p_{3/2}$ and $Cu2p_{1/2}$, respectively. The $Cu2p_{1/2}$ peaks are observed at a higher binding energy (approximately 20 eV) than the $Cu2p_{3/2}$ peaks due to spin-orbit coupling. Examination of the Cu2p spectrum reveals a significant difference between the peaks of $Cu^{2+}$ and $Cu^{1+}$ ions, as well as copper in its metallic state. According to previous studies, the Cu $2p_{3/2}$ binding energy ranges from 932.4 to 932.8 eV for $Cu_2O$ and metallic copper, while the $Cu2p_{1/2}$ peak lies at approximately 952.8 eV; the binding energy range for CuO has been reported to be 933.4-934.6 eV [61]. The Cu2p spectra of the monometallic catalyst indicate the presence of $Cu^{2+}$ at the surface layer. The broad satellite peak in the range of 940-945 eV, which was more visible in the case of the monometallic Cu/AC catalysts, indicates the existence of $Cu^{2+}$ ions in the form of cupric oxide, with a complex origin, due to multiple factors such as electron shake-up processes, charge transfer mechanisms, and final-state effects [60]. As the weight of nickel increases, this broad peak progressively disappears. The shake-up satellite peaks in the Cu2p spectra that emerged in the binding energy range of 940-945 eV are unique to $Cu^{2+}$ species and were not found in the profile of $Cu_2O$ or metallic copper ($Cu^0$) [61]. The Cu $2p_{3/2}$ and Cu $2p_{1/2}$ binding energies for the bimetallic catalysts differ slightly from those of Cu/AC, indicating that the chemical state of CuO was affected by the catalyst composition. It was previously suggested that as the catalyst composition changed, the electron density around the Cu atom also changed [60]. For the monometallic Cu/AC catalyst, the $Cu2p_{3/2}$ peak is visible at a binding energy of 933.5 eV, which is well within the range for CuO. The XPS profiles of the bimetallic catalysts show peaks at 932.6 eV and 952.4 eV, corresponding to $Cu2p_{3/2}$ and $Cu2p_{1/2}$, respectively. As observed from the graph, the intensity of the peaks first increases and then decreases with the addition of nickel. The peak positions of the bimetallic catalysts for both the $Cu2p_{3/2}$ and $Cu2p_{1/2}$ states also shifted toward lower binding energies compared to those of the monometallic catalysts. These results prove that on increasing the weight percentage of nickel, the $Cu^{2+}$ ions undergo partial reduction to $Cu^+$ ions or metallic copper, as evidenced by the disappearance of the satellite peaks discussed above [62].

Fig. 6(c) shows the Ni 2p XPS profiles of the freshly calcined catalysts. The monometallic Ni//AC catalyst exhibit two broad peaks at binding energies of 873.2 eV and 855.7 eV, attributed to the $Ni2p_{1/2}$ and $Ni2p_{3/2}$ states of $Ni^{2+}$, respectively, with a spin-orbit coupling energy of 17.5 eV [60-63]. The intensity of the peaks increases with the introduction of copper, confirming a synergistic interaction between nickel and copper [63]. An additional low-intensity shake-up satellite peak appears at 861.3 eV, which may be related to energy loss peaks caused by Plasmonian excitation in the metal [61]. These shake-up satellite peaks were observed in the XPS profiles of paramagnetic $Ni^{2+}$ compounds like NiO, $NiAl_2O_4$, $Ni(OH)_2$ etc., while the XPS profiles of diamagnetic $Ni^{3+}$ compounds and nickel metal ($Ni^0$) exhibited no such peaks [64]. Both monometallic and bimetallic catalysts exhibit two common peaks at roughly 531.8 eV and 285.1 eV, attributed to O1s and C1s, respectively. According to the literature, the C1s peak was identified at 285 eV, whereas the O1s peak was detected at 533 eV [64,65]. These peaks demonstrate the presence of carbon and oxygen atoms on the catalyst surface. The XPS profiles of Cu $2p_{3/2}$ and $2p_{1/2}$ for reduced catalysts are displayed in Fig. S1. The binding energies of $2p_{3/2}$ levels decrease to 932.3-932.7 eV and $2p_{1/2}$ level shows a binding energy between 952.3-952.5 eV. There are no satellite peaks, indicating that copper was reduced ($Cu^+$ or $Cu^0$). There is no distinction between binding energy values of $Cu^+$ and $Cu^0$. These findings reveal that copper was mostly present in the reduced samples in the form of $Cu^+$ and $Cu^0$. In addition, the XPS spectrum confirms the presence of Ni in all the reduced bimetallic catalyst samples. $Ni2p_{3/2}$ level shows a peak at binding energy value of 855.4 eV and $Ni2p_{1/2}$ level exhibits a peak at binding energy value of 873.1 eV. These two peaks are separated by spin-orbital splitting and confirm the presence of metallic nickel species ($Ni^0$).

**6. Scanning Electron Microscopy**

The morphology and crystal shape of the prepared catalysts were evaluated using scanning electron microscopy (SEM). Fig. 7(a)-(e) shows typical SEM images of the copper and nickel catalysts on the activated carbon support. All fresh catalysts comprised agglomerated, quasi-spherical nanoparticles, as shown in the figure. Particle agglomeration occurred during the calcination process due to sintering [21]. Copper particles are extensively distributed in the Cu/AC catalysts, where the smaller particles agglomerated into large particles. The crystallite size decreases as the nickel content in the catalysts increases, which may be attributed to the stabilizing effect caused by interaction of the metals [51]. The morphology changes when nickel is added, as found in bimetallic catalysts, confirming a synergistic interaction between Ni and Cu. The metal distribution on the surface of the activated carbon was evaluated by energy dispersive X-ray (EDX) elemental mapping, and the values are listed in Table 2.

**7. Catalyst Performance**

All the catalysts were tested in a continuous packed bed downflow reactor at a temperature, pressure, and WHSV of 220 °C, 0.75 MPa, and 0.97 $h^{-1}$, respectively. To achieve steady-state, the reac-

**Table 2. EDX elemental mapping data**

| Catalyst | Metal loading wt% | | Atomic % | |
|---|---|---|---|---|
| | Cu | Ni | Cu | Ni |
| Activated Carbon (AC) | - | - | - | - |
| Cu/AC | 17.4 | - | 4.0 | - |
| Cu-Ni(3 : 1)/AC | 20.9 | 5.5 | 5.3 | 1.5 |
| Cu-Ni(1 : 1)/AC | 16.3 | 12.5 | 4.25 | 3.5 |
| Cu-Ni(1 : 3)/AC | 15.3 | 17.6 | 4.05 | 5.06 |
| Ni/AC | - | 16.9 | - | 4.2 |

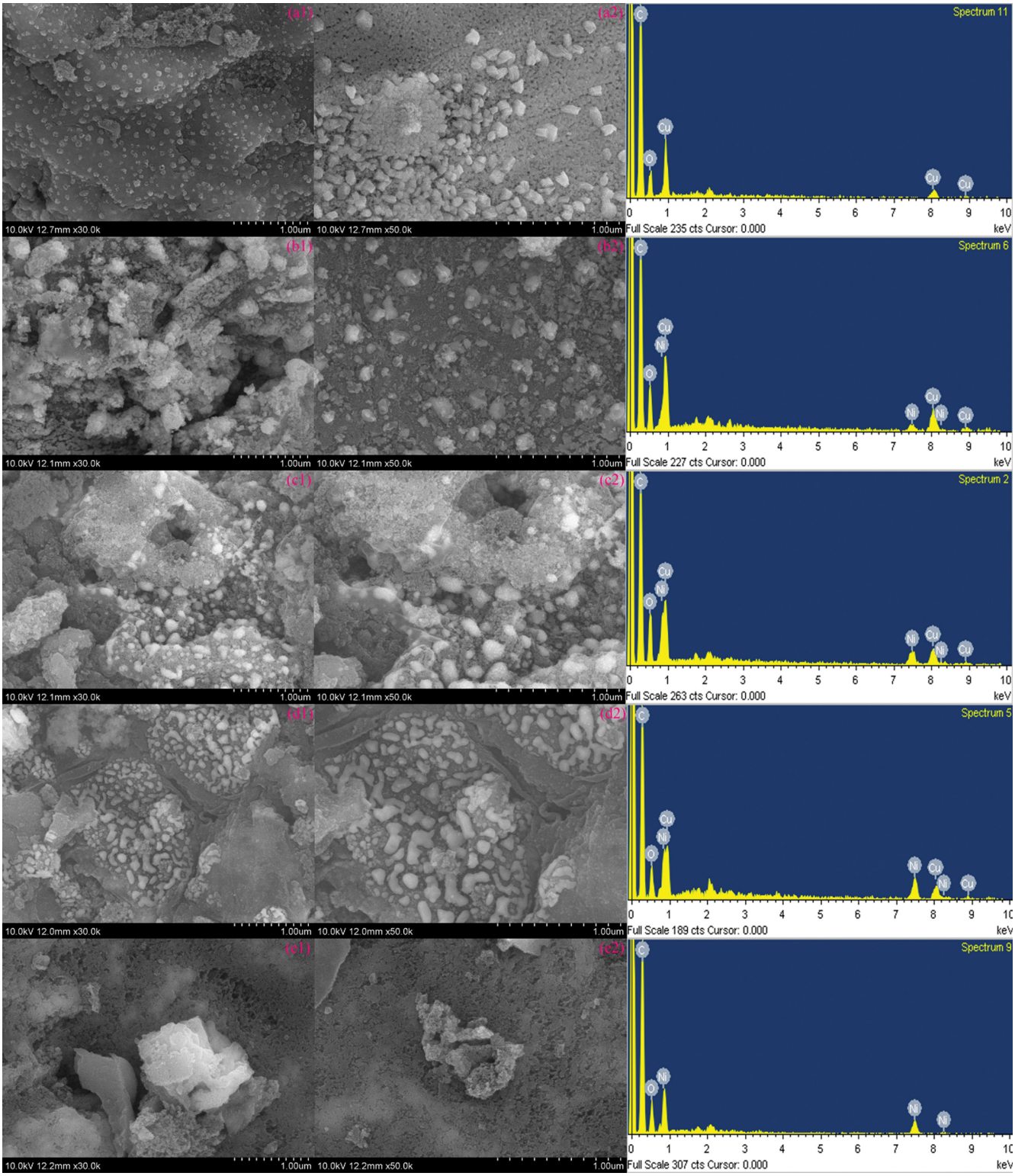


**Fig. 7. SEM images of the freshly calcined catalysts (a) Cu/AC, (b) Cu-Ni(3 : 1)/AC, (c) Cu-Ni(1 : 1)/AC, (d) Cu-Ni(1 : 3)/AC and (e) Ni/AC.**

tion was allowed to run continuously for 6 h after the liquid feed was initiated. The reaction was monitored every 2 h after steady-state was achieved. The glycerol conversion changed with time, although this variation was minimal after 14 h. As a result, all data for this experiment were collected after a run session of 14 h. Table 3 summarizes the performance of the catalysts under the aforementioned reaction conditions. The Cu/AC catalyst had the maximum glycerol conversion (97.2%), whereas conversion over the bimetallic catalysts was reported to be in the range of 73.5-95.7%. The catalytic activity declined as the nickel loading increased, with

**Table 3. Hydrogenolysis of glycerol over Cu-Ni/AC catalysts**

| Catalysts | Conversion (%) | Selectivity (%) | | | | 1,2-PDO yiled (%) |
|---|---|---|---|---|---|---|
| | | 1,2-PDO | Acetol | EG | Others* | |
| Cu/AC | 97.2 | 63.2 | 33.6 | 0 | 3.2 | 61.4 |
| Cu-Ni(3 : 1)/AC | 94.6 | 88.3 | 8.4 | 1.2 | 2.1 | 83.5 |
| Cu-Ni(1 : 1)/AC | 95.7 | 91.2 | 4.5 | 1.5 | 2.8 | 87.3 |
| Cu-Ni(1 : 3)/AC | 73.5 | 82.4 | 12.4 | 0.7 | 4.5 | 60.6 |
| Ni/AC | 12.2 | 26.7 | 45.7 | 3.4 | 24.2 | 3.3 |

Reaction condition: aqueous feed with 20 wt% glycerol, 220 °C; 0.75 MPa; 4 g catalyst, WHSV=0.97 $h^{-1}$; $H_2$/glycerol mole ratio=54.6.
Others*: 1-propanol, 2-propnaol, ethanol, and methanol

Ni/AC having the lowest activity. All the catalysts produced primarily 1,2-PDO and acetol, with trace amounts of EG, 2-PO, 1-PO, methanol, and ethanol. However, the amount of product obtained differed depending on the catalyst concentration. The selectivity of the Cu/AC catalyst for 1,2-PDO was determined to be 63.2%, where a considerable amount of acetol (33.6%) was also produced. Products such as EG and others were obtained in small quantities. These results corroborate those of Feng et al., who observed that strong acid sites facilitate the transformation of glycerol to acetol, as also supported by the $NH_3$-TPD results [60]. According to Mane et al., both acidic and metallic copper promote the dehydration of glycerol to acetol [66]. It was documented that glycerol hydrogenolysis is a combination of two reactions. The first reaction involves glycerol dehydration to an intermediate product, acetol, on the acidic sites, followed by hydrogenation of the intermediate (acetol) to 1,2-PDO over the active metal sites of the catalysts [10,11,33].

The products of the reaction over the Cu/AC catalysts confirm the simultaneous occurrence of dehydration and hydrogenation steps, with insignificant C-C bond cleavage. The Ni/AC catalysts showed the lowest conversion (12.2%) and selectivity for 1,2-PDO (26.7%), whereas the selectivity for acetol (45.7%), EG (3.4%), and other products (24.2%) was comparatively high. The formation of decomposition products, notably acetol and others, with Ni/AC suggests that the nickel catalyst preferentially promoted the dehydration of glycerol to acetol and C-C bond scission through an alternate reaction route. These results demonstrate the superior performance of copper catalysts over nickel catalysts in the hydrogenolysis reaction. All bimetallic catalysts yielded 1,2-PDO as the major product, with very low selectivity for acetol, EG, and other products. Cu-Ni(1 : 1)/AC afforded the maximum glycerol conversion (95.7%), whereas the other two bimetallic catalysts had slightly lower conversions of 94.6% and 73.5%, respectively. The bifunctional character of the catalysts and their high acid strength (1.26-3.83 mmol $NH_3$ g $cat^{-1}$) are associated with the high glycerol conversion [67,68]. The synergetic effect of copper and nickel in the bimetallic array and the small crystallite size may all play a role in maximizing the product yield. The bimetallic catalysts showed very high selectivity for 1,2-PDO, indicating that both dehydration and hydrogenation occurred simultaneously at a high rate because of the dual functionality of the catalysts. These findings further corroborate previous reports that the copper-nickel phase preferentially promoted scission of the C-O bond while suppressing C-C bond cleavage, resulting in a small amount of degradation products. The bimetallic Cu-Ni(1 : 1)/AC catalyst achieved the highest 1,2-PDO yield (87.3%) of all the catalysts evaluated for gas-phase glycerol hydrogenolysis. The high yield is due to the strong synergetic effect of the copper-nickel bimetal, smaller average crystallite size, and high acid strength. Given that the Cu-Ni(1 : 1)/AC catalyst achieved the maximum yield of 1,2-PDO, this catalyst was chosen for further evaluation.

**8. Determination of Reaction Parameters**

The effects of various reaction parameters, such as the reaction temperature, reaction pressure, and catalyst concentration, on the hydrogenolysis of glycerol over the Cu-Ni(1 : 1)/AC catalyst were examined to maximize the glycerol conversion and 1,2-PDO yield. The overall effect of these process variables on the conversion and product selectivity is described in the subsequent sections.

8-1. Reaction Temperature

The influence of temperature on the glycerol conversion and product selectivity over Cu-Ni(1 : 1)/AC was evaluated (Fig. 8(a)). There was no marked difference in the glycerol conversion (92.5-96%) over the temperature range of 220-300 °C. However, the yield of the major and minor products varied significantly with temperature. The selectivity for 1,2-PDO improved slightly at first, but then declined as the temperature increased, resulting in additional decomposition products. The yield of 1,2-PDO declined from 87.3% to 75.7% in the temperature range of 220-300 °C, with a substantial improvement in the selectivity for EG and other products. According to these observations, glycerol underwent excessive hydrogenolysis at higher temperatures due to breakage of the C-C bonds, resulting in decomposition products such as EG and lower alcohols [33,39,41]. The study further established that high temperatures were not favorable for glycerol hydrogenolysis.

8-2. Catalyst Amount

Fig. 8(b) illustrates the effect of the catalyst loading on the conversion and product selectivity over Cu-Ni(1 : 1)/AC at 220 °C. Increasing the catalyst loading from 1 g to 4 g led to a rapid increase in the conversion from 80.3% to 95.7%. However, increasing the catalyst loading induced a further relatively minimal increase in the glycerol conversion. Increasing the catalyst loading significantly boosted the number of active sites on the catalyst surface available for the reaction, resulting in higher conversion and 1,2-PDO selectivity [68]. The selectivity for 1,2-PDO increased from 84.5% to 91.2% when the catalyst loading increased from 1 g to 4 g. A higher catalyst loading (6 g) resulted in a significant reduction in

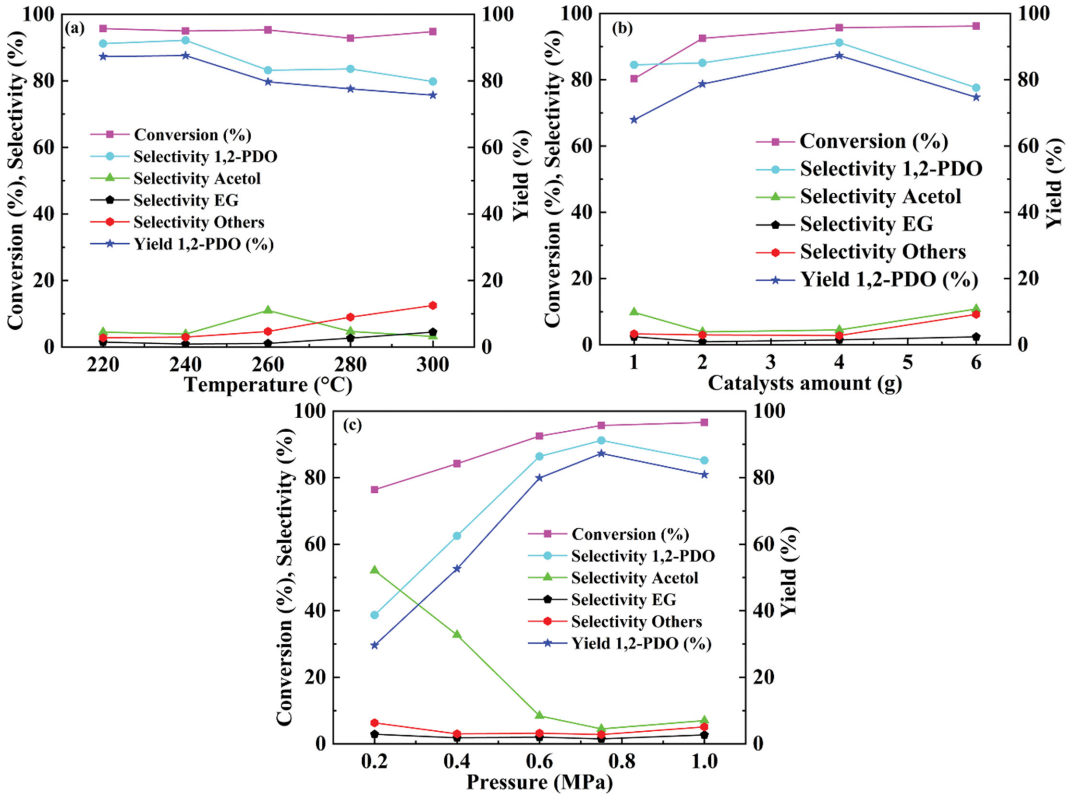


**Fig. 8. Variation of glycerol conversion and product selectivity over Cu-Ni(1 : 1)/AC (aqueous feed with 20 wt% glycerol, $H_2$ to glycerol mole ratio=54.6, reaction time=14 hours). (a) Effect of reaction temperature, 0.75 MPa, 4 g catalyst, WHSV=0.97 $h^{-1}$, (b) Effect of catalyst amount, 220 °C, 0.75 MPa, WHSV=0.97-1.11 $h^{-1}$, (c) Effect of reaction pressure, 220 °C, 4 g catalyst, WHSV=0.97 $h^{-1}$.**

the selectivity for 1,2-PDO (77.6%), in addition to an increase in EG and a lower alcohol concentration in the product stream. Increasing the catalyst loading resulted in excess hydrogenolysis to degradation products owing to the abundance of active sites on the catalyst surface. Because the maximum 1,2-PDO yield (87.3%) was achieved with 4 g catalyst, this catalyst loading was chosen for further study.

8-3. Reaction Pressure

It was previously established that the reaction pressure has a profound effect on the conversion and product yield. The effect of hydrogen pressure on the glycerol conversion and yield of different products over Cu-Ni(1 : 1)/AC was examined within the pressure range of 0.2-1.0 MPa, with a uniform temperature of 220 °C, 4 g catalyst, WHSV value of 0.97 $h^{-1}$, and uniform mole ratio ($H_2$ to glycerol) of 54.6. Fig. 8(c) shows the results. With a pressure increase from 0.2 to 0.75 MPa, the conversion increased significantly from 76.4% to 95.7% and remained nearly constant above 0.75 MPa. The transformation of acetol to 1,2-PDO increased, resulting in reduced selectivity to acetol at higher pressure because of an increase in the concentration of active hydrogen species due to the reaction over the metallic sites. The selectivity for acetol declined significantly from 52.1% to 7%, while the selectivity for 1,2-PDO increased significantly from 38.7% to 91.2% in the pressure range of 0.2-0.75 MPa. The change in the selectivity for the minor products was minimal (2.8-5.1%). These results demonstrate the formation of acetol as a reaction intermediate, which was further hydrogenated at a higher reaction pressure to give 1,2-PDO [30,39, 41]. These findings also reveal that due to the abundance of hydrogen atoms, lower pressure favored the transformation of glycerol to acetol, but higher pressure favored the hydrogenation of acetol to 1,2-PDO [39]. The selectivity for 1,2-PDO declined due to the excessive decomposition of 1,2-PDO to smaller alcohols at higher pressures (>0.75 MPa). The overall output of 1,2-PDO surged approximately three-fold from 29.6% to 87.3% with an increase in pressure.

## CONCLUSIONS

Various Cu and Ni mono- and bimetallic catalysts produced by the incipient wetness impregnation technique demonstrated remarkable catalytic behavior in the hydrogenolysis of glycerol in the gaseous phase. The amount of copper and nickel in the catalysts significantly affected their physicochemical features, catalytic performance, and 1,2-PDO selectivity. The major products of the hydrogenolysis reaction were 1,2-PDO and acetol, with trace amounts of other products such as EG, 1-PO, and 2-propanol. The Cu catalyst achieved a conversion of 97.2% with a 1,2-PDO selectivity of 63.2%, whereas the Ni catalyst showed a conversion of 12.2% with a 1,2-PDO yield of 3.3%. A high percentage of degradation products (24.2%) was formed over the nickel catalysts, suggesting excessive hydrogenolysis of glycerol to lower alcohols. The catalytic performance and 1,2-PDO selectivity of the bimetallic catalysts excelled

those of the monometallic catalysts due to the bifunctional nature of the former. Cu-Ni(1 : 1) showed the best catalytic performance and product selectivity of all the Cu-Ni bimetallic catalysts, achieving the highest 1,2-PDO yield of 87.3% at 0.75 MPa and 220 °C, with a $H_2$/glycerol mole ratio of 54.6 and WHSV of 0.97 $h^{-1}$. The remarkable performance of the Cu-Ni(1 : 1)/AC catalyst is due to the strong synergy between the Cu-Ni bimetal and the activated carbon, high acid strength, and small crystallite size. The results demonstrate that Cu-Ni catalysts facilitate C-O bond scission instead of C-C bond breakage, inhibiting byproduct formation and suggesting a dehydration-hydrogenation pathway for the reaction. Analysis of the reaction parameters for the Cu-Ni(1 : 1)/AC catalyst indicated a maximum 1,2-PDO yield of 87.3% under mild reaction conditions of 220 °C, 0.75 MPa, and WHSV of 0.97 $h^{-1}$.

## ACKNOWLEDGEMENTS

This research was supported by the Korean Ministry of Trade, Industry, and Energy (Project number: 20008490). The authors acknowledge the Department of Science and Technology (DST), Government of India for financial support under the FTYS scheme.

## SUPPORTING INFORMATION

Additional information as noted in the text. This information is available via the Internet at http://www.springer.com/chemistry/journal/11814.

## REFERENCES

1. Renewable energy policy Network 21st Century steering committee. Renewables 2021: global status report. https://www.ren21.net/wp-content/uploads/2019/05/GSR2021_Full_Report.pdf.
2. OECD/FA, OECD-FAO Agricultural Outlook 2018-2027. Paris, Rome, OECD Publishing, FAO (2018).
3. M. Ayoub and A. Z. Abdullah, *Renew. Sustain. Energy Rev.*, **16**, 2671 (2012).
4. F. Yang, M. A. Hanna and R. Sun, *Biotechnol. Biofuels*, **5**, 1 (2012).
5. S. Bagheri, N. M. Julkapli and W. A. Yehye, *Renew. Sustain. Energy Rev.*, **41**, 113 (2015).
6. C. A. G. Quispe, C. J. R. Coronado and J. A. Carvalho, *Renew. Sustain. Energy Rev.*, **27**, 475 (2013).
7. Y. Wang, J. Zhou and X. Guo, *RSC Adv.*, **5**, 74611 (2015).
8. A. Brandner, K. Lehnert, A. Bienholz, M. Lucas and P. Claus, *Top. Catal.* **52**, 278 (2009).
9. A. Marinas, P. Bruijnincx, J. Ftouni, F. J. Urbano and C. Pinel, *Catal. Today*, **239**, 31 (2015).
10. T. Miyazawa, Y. Kusunoki, K. Kunimori and K. Tomishige, *J. Catal.*, **240**, 213 (2006).
11. J. Hu, X. Liu, B. Wang, Y. Pei, M. Qiao and K. Fan, *Chin. J. Catal.*, **33**, 1266 (2012).
12. C. Montassier, D. Giraud, J. Barbier, M. Guisnet, J. Barrault, C. Bouchoule, D. Duprez, C. Montassier and G. Perot, *Heter. Catal. Fine Chem.*, Elsevier, 165 (1988).
13. J. Feng, H. Fu, J. Wang, R. Li, H. Chen and X. Li, *Catal. Commun.*, **9**, 1458 (2008).
14. S. Wang, K. Yin, Y. Zhang and H. Liu, *ACS Catal.*, **3**, 2112(2013).
15. Y. Nakagawa and K. Tomishige, *Catal. Sci. Technol.* **1**, 179 (2011).
16. C. Montassier, J. C. Menezo, L. C. Hoang, C. Renaud and J. Barbier, *J. Mol. Catal.* **70**, 99 (1991).
17. D. G. Lahr and B. H. Shanks, *J. Catal.*, **232**, 386 (2005).
18. R. Mane, S. Patil, M. Shirai, S. Rayalu and C. Rode, *Appl. Catal. B: Environ.*, **204**, 134 (2017).
19. I. Furikado, T. Miyazawa, S. Koso, A. Shimao, K. Kunimori and K. Tomishige, *Green Chem.*, **9**, 582 (2007).
20. Y. Nakagawa, Y. Shinmi, S. Koso and K. Tomishige, *J. Catal.*, **272**, 191 (2010).
21. S. M. Pudi, P. Biswas, S. Kumar and B. Sarkar, *J. Braz. Chem. Soc.*, **26**, 1551 (2015).
22. C. T. Q. Mai and F. T. T. Ng, *Catal. Today*, **291**, 195 (2017).
23. H. Tan, M. N. Hedhill, Y. Wang, J. Zhang, K. Li, S. Sioud, Z. A. Al-Talla, M. H. Amad, T. Zhan, O. E. Tall and Y. Han, *Catal. Sci. Technol.*, **3**, 3360 (2013).
24. J. Zheng, W. Zhu, C. Ma, Y. Hou, W. Zhang and Z. Wang, *React. Kinet. Mech. Catal.*, **99**, 455 (2010).
25. S. K. Tanielyan, N. Marin, G. Alvez, R. Bhagat, B. Miryala, R. L. Augustine and S. R. Schmidt, *Org. Process Res. Dev.*, **18,** 1419 (2014).
26. H. Zhao, L. Zheng, X. Li, P. Chen and Z. Hou, *Catal. Today*, **355**, 84 (2020).
27. Z. Yuan, J. Wang, L. Wang, W. Xie, P. Chen, Z. Hou and X. Zheng, *Bioresour. Technol.*, **101,** 7088 (2010).
28. Z. Wu, Y. Mao, M. Song, X. Yin and M. Zhang, *Catal. Commun.*, **32**, 52 (2013).
29. S. M. Pudi, P. Biswas and S. Kumar, *J. Chem. Technol. Biotechnol.*, **91**, 2063 (2016).
30. N. N. Pandhare, S. M. Pudi, P. Biswas and S. Sinha, *Org. Process Res. Dev.*, **20**, 1059 (2016).
31. N. N. Pandhare, S. M. Pudi, P. Biswas and S. Sinha, *J. Taiwan Inst. Chem. Eng.*, **61**, 90 (2016).
32. A. Bienholz, H. Hofmann and P. Claus, *Appl. Catal. A: Gen.*, **391**, 153 (2011).
33. S. Sato, M. Akiyama, R. Takahashi, T. Hara, K. Inui and M. Yokota, *Appl. Catal. A: Gen.*, **347**, 186 (2008).
34. D. Sun, Y. Yamada, S. Sato and W. Ueda, *Appl. Catal. B: Environ.*, **193**, 75 (2016).
35. D. Sun, Y. Yamada and S. Sato, *Appl. Catal. A: Gen.*, **475**, 63 (2014).
36. Z. Yuan, P. Wu, J. Gao, X. Lu, Z. Hou and X. Zheng, *Catal. Lett.*, **130**, 261 (2009).
37. L. Zheng, S. Xia and Z. Hou, *Appl. Clay Sci.*, **118**, 68 (2015).
38. Z. Yuan, L. Wang, J. Wang, S. Xia, P. Chen, Z. Hou and X. Zheng, *Appl. Catal. B: Environ.*, **101**, 431 (2011).
39. D. K. Pandey and P. Biswas, *React. Chem. Eng.*, **5**, 2221 (2020).
40. L. Huang, Y. L. Zhu, H. Y. Zheng, Y. W. Li and Z. Y. Zeng, *J. Chem.Technol. Biotechnol.*, **83**, 1670 (2008).
41. M. Akiyama, S. Sato, R. Takahashi, K. Inui and M. Yokota, *Appl. Catal. A: Gen.*, **371**, 60 (2009).
42. S. Zhu, X. Gao, Y. Zhu, H. Zheng and Y. Li, *J. Catal.*, **303**, 70 (2013).
43. J. Zhao, W. Yu, C. Chen, H. Miao, H. Ma and J. Xu, *Catal. Lett.*, **134**, 184 (2010).
44. I. Jiménez-Morales, F. Vila, R. Mariscal and A. Jiménez-López, *Appl.*

*Catal. B: Environ.*, **117-118**, 253 (2012).
45. O. S. G. P. Soares, J. J. M. Órfão and M. F. R. Pereira, *Appl. Catal. B: Environ.*, **91**, 441 (2009).
46. O. S. G. P. Soares, J. J. M. Órfão and M. F. R. Pereira, *Catal. Lett.*, **126**, 253 (2008).
47. T. J. Bandosz, in *Surface chemistry of carbon materials*, P. Serp, J. L. Figueiredo Eds., Carbon Materials for Catalysis, J. Wiley & Sons, Hoboken, NJ (2009).
48. F. Rodríguez-Reinoso, *Carbon*, **36**, 159 (1988).
49. E. G. Suarez, A. G. Ruiz, I. R. Ramos and A. Arcoya, *Chem. Eng. J.*, **262**, 326 (2015).
50. M. Kruk and M. Jaroniec, *Chem. Mater.*, **13**, 3169 (2001).
51. G. Leofanti, M. Padovan, G. Tozzola and B. Venturelli, *Catal. Today*, **41**, 207 (1998).
52. P. K. Vanama, A. Kumar, S. R. Ginjupalli and V. R. C. Komandur, *Catal. Today*, **250**, 226 (2015).
53. I. Gandarias, J. Requies, P. L. Arias, U. Armbruster and A. Martin, *J. Catal.*, **290**, 79 (2012).
54. B. Zhang, H. You, F. Wang and Z. Yang, *Catal. Commun.*, **88**, 56 (2017).
55. H. Tüysüz, E. L. Salabaş, E. Bill, H. Bongard, B. Spliethoff, C. W. Lehmann and F. Schüth, *Chem. Mater.*, **24**, 2493 (2012).
56. R. Hierl, H. Knözinger and H. P. Urbach, *J. Catal.*, **69**, 475 (1981).
57. R. Merabti, K. Bachari, D. Halliche, Z. Rassoul and A. Saadi, *React. Kinet. Mech. Catal.*, **101**, 195 (2010).
58. O. Arbeláez, T. R. Reina, S. Ivanova, F. Bustamante, A. L. Villa, M. A. Centeno and J. A. Odriozola, *Appl. Catal. A: Gen.*, **497**, 1 (2015).
59. N. Khandan, M. Kazemeini and M. Aghaziarati, *Appl. Catal. A: Gen.*, **349**, 6 (2008).
60. Y. Feng, H. Yin, A. Wang, L. Shen, L. Yu and T. Jiang, *Chem. Eng. J.*, **168**, 403 (2011).
61. S. A. Khromova, A. A. Smirnov, O. A. Bulavchenko, A. A. Saraev, V. V. Kaichev, S. I. Reshetnikov and V. A. Yakovlev, *Appl. Catal. A: Gen.*, **470**, 261 (2014).
62. P. F. Barbieri, A de Siervo, M. Carazzolle, R. Landers and G. G. Kleiman, *J. Electron. Spectros. Relat. Phenomena*, **135**, 113 (2004).
63. L. Huang, Y. Lv, S. Wu, P. Liu, W. Xiong, F. Hao and H. Luo, *Appl. Catal. A: Gen.*, **577**, 76 (2019).
64. V. V. Kaichev, A. Y. Gladky, I. P. Prosvirin, A. A. Saraev, M. Hävecker, A. Knop-Gericke, R. Schlogl and V. I. Bukhtiyarov, *Surf. Sci.*, **609**, 113 (2013).
65. S. P. Patil, J. V. Pande and R. B. Biniwale, *Int. J. Hydrogen Energy*, **38**, 15233 (2013).
66. R. B. Mane, A. Yamaguchi, A. Malawadkar, M. Shirai and C. V. Rode, *RSC Adv.*, **3**, 16499 (2013).
67. M. Balaraju, V. Rekha, B. L. A. P. Devi, P. S. S. Prasad, R. B. N. Prasad and N. Lingaiah, *Appl. Catal. A: Gen.*, **354**, 82 (2009).
68. R. B. Mane, A. M. Hengne, A. A. Ghalwadkar, S. Vijayanand, P. H. Mohite, H. S. Potdar and C. V. Rode, *Catal. Lett.*, **135**, 141 (2010).
69. N. Riaz, F. K. Chong, B. K. Dutta, Z. B. Man, M. S. Khan and E. Nurlaela, *Chem. Eng. J.*, **185-186**, 108 (2012).

# Supporting Information

# Vapor-phase hydrogenolysis of glycerol to value-added 1,2-propanediol over copper-nickel bimetallic catalysts supported on activated carbon

**Mohammad Kashif*, Sadhasivam Thangarasu*, Tae Hwan Oh*,†, Prakash Biswas**, and Dohyung Kang***

*School of Chemical Engineering, Yeungnam University, Gyeongsan 38541, Korea
**Department of Chemical Engineering, Indian Institute of Technology Roorkee, 247667 Roorkee, Uttarakhand, India
(*Received 21 January 2022 • Revised 30 May 2022 • Accepted 2 June 2022*)

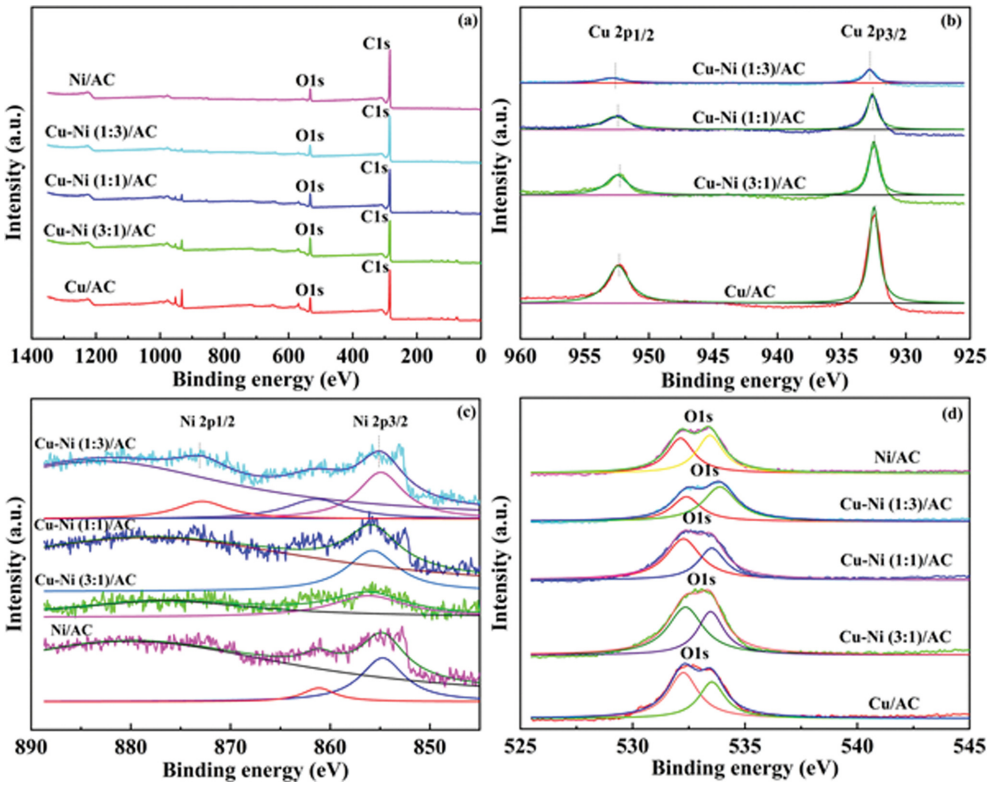


**Fig. S1. (a) XPS data of reduced catalysts, deconvoluted XPS spectra of (b) Cu2p peaks, (c) Ni2p peaks, and (d) O1s peak.**


**Fig. S2. SEM image of Cu-Ni(1 : 1)/AC catalyst.**